CHAPTER 5

Performance Enhancement of TiO_2-encapsulated Photoelectrodes Based on III–V Compound Semiconductors

YU WANG[a] AND STEPHEN B. CRONIN*[b]

[a] Mork Family Department of Chemical Engineering and Materials Science, University of Southern California, Los Angeles, CA 90089, USA; [b] Ming Hsieh Department of Electrical Engineering, Department of Chemistry, and Department of Physics and Astronomy, University of Southern California, Los Angeles, CA 90089, USA
*Email: scronin@usc.edu

5.1 Introduction

The intermittence of solar energy presents a serious challenge when trying to incorporate a high percentage of solar power into the electric power grid. To solve this problem, photoelectrochemical (PEC) water splitting and CO_2 reduction can be used to store solar energy in the form of chemical bonds that can be released later. Although the use of TiO_2 alone in water splitting under UV light irradiance has been demonstrated, its band gap is too wide ($E_g = 3.2$ eV) for it to be used for efficient solar energy conversion.[1] Based on the Shockley–Queisser limit, the band gap of a semiconductor should be in the range 1.2–1.4 eV for optimum solar power utilization.[2] Various III–V compound semiconductors, such as GaAs, GaP, and InP, are promising candidates,

Energy and Environment Series No. 30
Ultrathin Oxide Layers for Solar and Electrocatalytic Systems
Edited by Heinz Frei and Daniel V. Esposito

Published by the Royal Society of Chemistry, www.rsc.org

and their theoretical photocurrent densities are much higher than that of TiO_2 alone under one-sun illumination.[3] However, these semiconductors are not stable and often undergo photocorrosion in the photocatalytic production of solar fuels.

Figure 5.1a,b show the optical microscopy and atomic force microscopy (AFM) images of a bare p-type GaP photocathode after 8 h of CO_2 reduction reaction in CO_2-saturated 0.5 M NaCl aqueous solution under 532 nm light illumination.[4] The surface of the bare GaP substrate changed color and became rougher. The root mean square (RMS) roughness is about ±54 nm (shown in Figure 5.1c). It is desirable to provide a thin and pinhole-free oxide layer to protect the underlying photoelectrode while not preventing charge transfer. Atomic layer deposition (ALD) is a powerful tool to facilitate these goals because it can provide a conformal oxide layer with thickness control at the ångström level. McIntyre's group first demonstrated that 2 nm TiO_2 surface coatings grown by ALD can prevent the corrosion of a silicon photoanode from the oxygen evolution reaction (OER) while allowing electrons to tunnel through, and they are sufficiently transparent in the visible wavelength range.[5] Later, the protection of a nanotextured p-type InP photocathode by a TiO_2 passivation layer in the hydrogen evolution reaction (HER) was demonstrated.[6]

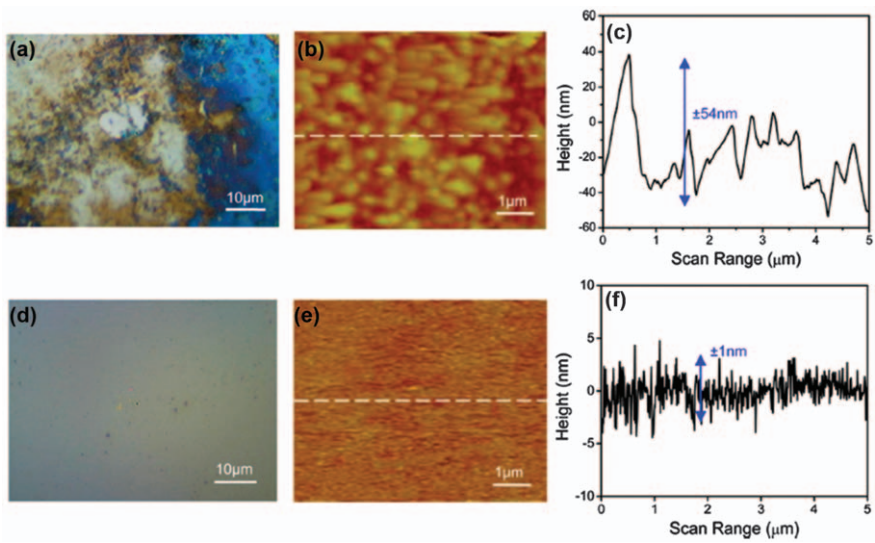

Figure 5.1 (a) Optical microscopy image, (b) atomic force microscopy (AFM) image, and (c) surface topography of the surface of a bare p-type GaP photocathode after 8 h of CO_2 reduction reaction at an applied potential of −0.5 V *vs.* NHE in CO_2-purged 0.5 M NaCl solution under 532 nm laser illumination. (d) Optical microscopy, (e) AFM, and (f) surface topography of the surface of a GaP photocathode passivated with a 5 nm TiO_2 layer after 8 h of CO_2 reduction reaction.
Reproduced from ref. 4 with permission from American Chemical Society, Copyright 2014.

As Figure 5.1d,e show, upon 5 nm TiO_2 passivation, the GaP surface is stable with a uniform color after 8 h of CO_2 reduction reaction, and the RMS roughness is only ± 1 nm (shown in Figure 5.1f). The change in the morphology and appearance of as-fabricated TiO_2–GaP photocathodes is minimal before and after the reaction. In addition, Ti^{3+} surface states, which originate from oxygen vacancies, can lower the binding energy of reactant molecules and intermediates,[6–9] and the built-in electric field formed between n-type TiO_2 film and p-type III–V semiconductors can enhance the charge separation process for photogenerated electron–hole pairs.[10] Therefore, by passivating III–V compound semiconductors with TiO_2 films, strongly absorbing materials can be combined with highly catalytic materials to achieve efficient and stable solar energy conversion.

5.2 Fabrication, Characterization, and Surface States of TiO_2 Layers

5.2.1 Fabrication Methods

ALD provides a facile deposition technique for producing thin films of various materials, from metal oxides to noble metals.[11,12] During the deposition, the target substrate is kept in a vacuum chamber under a pressure of <1 Torr, and is exposed alternately to pulses of each chemical precursor. In each half-reaction, an individual source is pulsed into the reaction chamber for a certain amount of time to form one monolayer of part of the target material through a self-saturating process. Then, a carrier gas such as nitrogen or argon is purged into the chamber to eliminate unreacted precursor or by-products, followed by the pulse and purge of another chemical precursor. This process is repeated until the desired thickness of the target material is achieved.[11] For a TiO_2 layer, $TiCl_4$ or tetrakis(dimethylamido)titanium (TDMAT) is used as a titanium source and water is used as an oxygen source.[5,7,13,14] There are several advantages of ALD over other chemical vapor deposition (CVD) or physical vapor deposition (PVD) methods. First, the as-deposited film is conformal and pinhole free because of its self-limiting characteristics. Second, the thickness can be controlled at the ångström level because of its cycle-by-cycle deposition nature so that the as-deposited film can be made very thin and precise.[11] These two properties are critical for protecting the underlying semiconductor photoelectrodes while not inhibiting charge transfer in PEC processes. Although the deposition rate is very slow compared with other deposition methods, only a few nanometers thick TiO_2 layer is needed to achieve the optimal PEC performances of these photoelectrodes.[6,7,9,15]

5.2.2 Characterization Methods

The as-deposited TiO_2 films can be characterized by several experimental methods, including high-resolution transmission electron microscopy (HRTEM), electron energy-loss spectroscopy (EELS), and X-ray photoemission

spectroscopy (XPS). HRTEM is used to analyze the film morphology and crystallinity, and the spatial chemical composition profile can be extracted by EELS. Figure 5.2a–c show typical HRTEM images of ALD-deposited TiO_2 films with 25, 75, and 500 deposition cycles at 250 °C on p-type GaAs substrates.[8] During the deposition, $TiCl_4$ is used for the first half-cycle as the Ti source, followed by water vapor as the O source. Figure 5.2d–f show the EELS spatial profiles of Ti and O species corresponding to different numbers of deposition cycles. For 25-cycle depositions (shown in Figure 5.2a), the oxygen signal increases 0.5 nm before the Ti signal, which indicates that the native GaAs oxide still exists below the TiO_2 film. However, the native oxide of GaAs is removed by the TiO_2 film with 75 cycles of deposition (shown in Figure 5.2b). The reason for this is that Cl^- ions from the $TiCl_4$ precursor partially removed GaAs native oxide after 25 cycles. This is further verified by the EELS spatial maps in Figure 5.2e, showing that both the O and Ti signals together increase in the same position for the 75-cycle deposition. With 500 cycles of ALD deposition, the TiO_2 film forms a crystalline structure with an interplane distance of 3.5 ± 0.1 Å (shown in Figure 5.2c). Thick crystalline TiO_2 will greatly inhibit charge transfer owing to its wide band gap and insulating nature, thus offering no improvement in photocatalytic performance for III–V compound semiconductors unless it is thin enough (<2 nm) to allow electrons to tunnel through.[14] Hu *et al.* also showed that unannealed TiO_2 coatings up to 143 nm thick can still maintain their amorphous, highly conductive, and transparent natures, while preventing corrosion for Si, GaAs, and GaP photoanodes during water oxidation reactions in 1 M KOH solution. In that work, they used

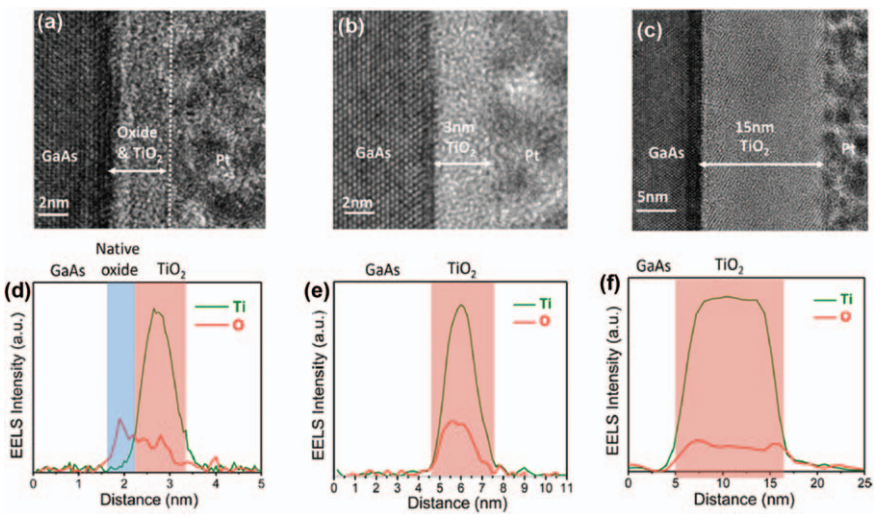

Figure 5.2 HRTEM images of TiO_2 passivation films with (a) 25, (b) 75, and (c) 500 cycles of ALD deposition on p-type GaAs substrates. EELS spatial maps of Ti L edge and O K edge for (d) 25, (e) 75, and (f) 500 ALD deposition cycles. Reproduced from ref. 8 with permission from American Chemical Society, Copyright 2015.

a lower deposition temperature (150 °C) and different Ti precursor [tetrakis(dimethylamido)titanium (TDMAT)] in their ALD process.[16]

5.2.3 Catalytic Outer Surface States

Ti^{3+} defect states on the surface of amorphous TiO_2 films can lower the potential barrier and promote charge transfer, thus enhancing the PEC performance of III–V compound semiconductors. In order to quantify the importance of those defect states, plane wave density function theory (PW-DFT) has been used to calculate the adsorption energy of CO_2 and H_2O molecules adsorbed on the TiO_2 surface. Figure 5.3a shows the anatase TiO_2 structure used in the PW-DFT calculation by Alexandrova's group,[7,8] and the adsorption energy is calculated based on the following equation:

$$E_{ads} = E[\text{surf} + \text{molecule}] - E[\text{surf}] - E[\text{molecule}] \tag{5.1}$$

Both stoichiometric and defective anatase (with an oxygen vacancy) were analyzed in their study (only defective anatase is shown in Figure 5.3). Relevant to the HER, E_{ads} is −1.26 and −1.50 eV for a neutral H_2O molecule adsorbed on stoichiometric and defective anatase, respectively. The O atom in the H_2O molecule tends to fill the oxygen vacancy, and the two H atoms

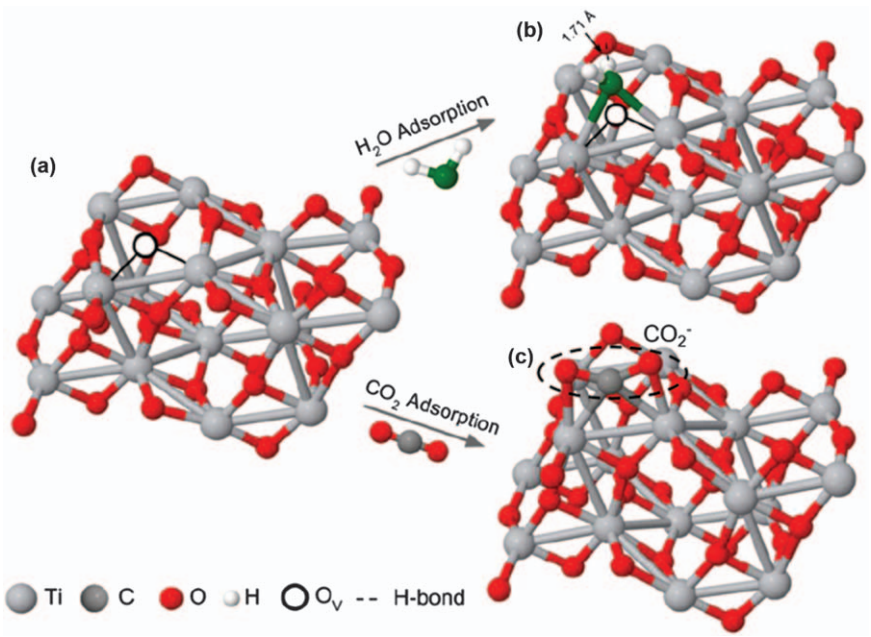

Figure 5.3 Defective anatase structure used in PW-DFT calculation with oxygen vacancies (a) before adsorption, (b) after H_2O molecule adsorption and relaxation, and (c) after CO_2 molecule adsorption and relaxation. Adapted from ref. 8 with permission from American Chemical Society, Copyright 2015.

form hydrogen bonds with the neighboring surface oxygens on the TiO_2 film.[8] For the CO_2 reduction reaction, the calculation shows that E_{ads} is −0.48 eV for stoichiometric anatase and −0.94 eV for defective anatase. In addition, the linear CO_2 molecule becomes bent when it occupies the bridging oxygen vacancy, as shown in Figure 5.3c. Upon adsorption, the calculation also shows that CO_2 gains an electron (−0.897e) from the TiO_2 substrate spontaneously, meaning that no overpotential is required to form CO_2^- intermediates that can subsequently form methanol and CO in aqueous and non-aqueous electrolytes.[7,9]

5.2.4 Quantifying Surface States

The density of defective states in TiO_2 overlayers can be characterized by XPS. Figure 5.4 shows the typical XPS spectra of different thicknesses of TiO_2 films deposited on GaAs surfaces.[13] Here, the core-level binding energies of Ti $2p_{1/2}$ and Ti $2p_{3/2}$ are 464.7 and 459.0 eV, respectively (Figure 5.4a). Additionally, the lower binding energy of 457.1 eV corresponds to Ti^{3+} states, and the area ratios of Ti^{3+} to Ti $2p_{1/2}$ are 0.15, 0.09, and 0.061 for the 1, 3, and 5 nm thick TiO_2 films, respectively. This indicates a higher density of defective states in thinner TiO_2 films. As will be shown in later sections, thinner TiO_2 films also have better

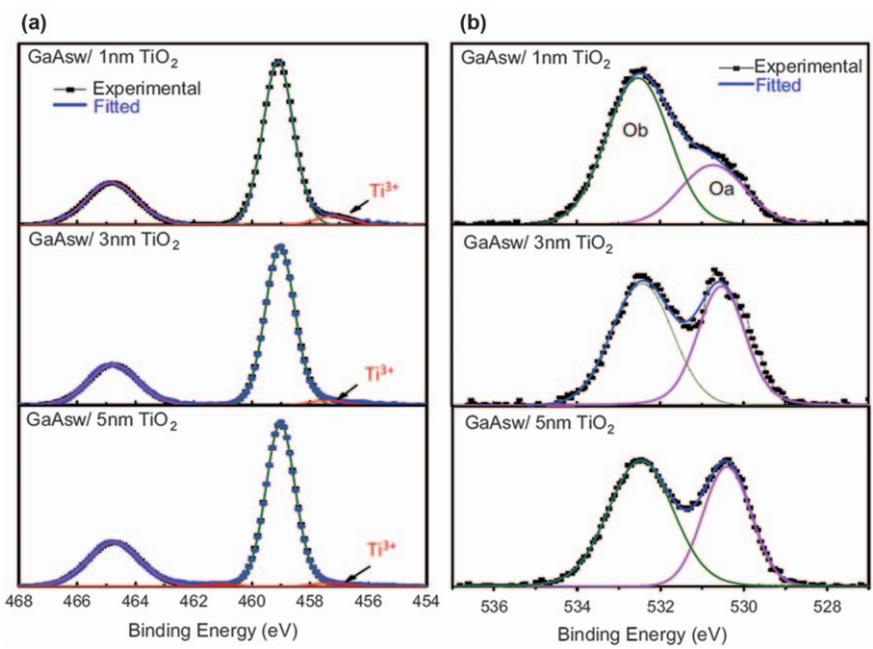

Figure 5.4 (a) Ti 2p and (b) O 1s core-level XPS spectra of different thicknesses of TiO_2 films on p-type GaAs substrates.
Reproduced from ref. 13 with permission from Elsevier, Copyright 2016.

performance in photocatalytic reactions, such as water splitting and CO_2 reduction. Furthermore, two O peaks are shown in Figure 5.4b, originating from TiO_2 layers. Two symmetrical Gaussian peaks are fitted from experimental data, which are denoted Oa and Ob from the O 1s core level.[17] For a 1 nm TiO_2-encapsulated GaAs substrate, the native oxide may contribute to the O 1s peaks. For 3 and 5 nm thick TiO_2-encapsulated substrates, the native oxide is removed by the ALD process as indicated in Figure 5.2. The Oa peak results from O atoms from stoichiometric TiO_2 and the Ob peak is attributed to oxygen vacancies. The area ratios between the Ob and Oa peaks are 2.4, 1.6, and 1.4 for 1, 3, and 5 nm thick TiO_2 films, respectively; therefore, the density of oxygen vacancies also increases as the TiO_2 layer becomes thinner.

5.3 Photocatalytic Enhancement of TiO_2-encapsulated III–V Semiconductors

5.3.1 InP

InP has a direct band gap of ~1.35 eV and is suitable for the optimum utilization of the terrestrial solar spectrum according to the Shockley–Quiesser limit.[2] It has surface-recombination velocities of 10^4 and 10^5 cm s^{-1} for n- and p-type, respectively, which are low compared with other III–V semiconductors.[18] Also, the optical absorption of InP is high and can be further enhanced by nanotexturing technique.[6,7,19] Low surface-recombination velocities combined with high optical absorption will lead to a pronounced short-circuit current density (up to 37 mA cm^{-2} in a proton reduction reaction).[6] Furthermore, it has a desirable position of the conduction band edge with respect to H^+/H_2 and CO_2/CO_2^- redox potentials, thereby making Zn-doped p-type InP a suitable photocathode in water splitting and CO_2 reduction reactions. The cost of InP can be further reduced by using a non-epitaxial grown thin-film substrate rather than single-crystalline wafers.[15] Aharon-Shalom and Heller demonstrated the HER using p-type InP (Rh–H alloy) and p-type InP (Re–H alloy) as photocathodes in 1982.[20] In their findings, the applied bias photon-to-current efficiencies (ABPE) were 13.3 and 11.4%, respectively. ABPE used here is calculated based on the comparison between the applied potential at photocathodes and the thermodynamic potential generated from an ideal fuel cell cathode:[21]

$$\eta = \left[\frac{\left(V_{\mathrm{App}} - V_{\mathrm{H_2}}\right) \times J}{P_0}\right] \times 100\% \tag{5.2}$$

where V_{App} is the applied potential at photocathodes *vs.* RHE, $V_{\mathrm{H_2}}$ is the reduction potential of H^+/H_2 *vs.* RHE (which is 0 V here), J is the cell output current density, and P_0 is the incident light power density. However, InP is not stable and undergoes photocorrosion in aqueous solutions. A TiO_2 encapsulation layer grown by ALD can be used to address this problem because

of its chemical stability and high uniformity. In addition, n-type TiO_2 has a large offset in the valence band edge compared with p-type InP, which induces an energy barrier for holes in InP to reach the TiO_2 surface and reduces interface electron–hole recombination.[22] This decrease in recombination will enable a higher photovoltage to be generated and lead to a positive onset potential shift for the photocathode that makes the design of tandem cells for unassisted water splitting possible in the future. Also, the conduction band of InP is well aligned with respect to that of TiO_2, and the built-in electric field between p-type InP and n-type TiO_2 also assists electron extraction while repelling holes. The combination of all these effects makes the TiO_2-passivated p-type InP substrate a highly electron-selective photocathode for reduction reactions. Depositing co-catalysts on top of TiO_2 will further enhance the photoelectrochemical performance by decreasing kinetic overpotential losses. We discuss the performance of the p-type InP photocathode in the HER and CO_2 reduction separately in detail below.

Figure 5.5 shows a comparison of the photoelectrochemical HER performance of p-type InP with a doping level of $3–5\times10^{17}\,cm^{-3}$ with and without the TiO_2 encapsulation layer in 1 M $HClO_4$ solution under AM1.5 simulated solar spectra, reported by Lin *et al.*[10] Here, the TiO_2 film was deposited by ALD with a 10 nm thickness at 250 °C, and titanium isopropoxide and water were used as precursors. The surface of the as-deposited TiO_2 film was treated by 2 nm Pt sputtering as a co-catalyst. Figure 5.5a shows the measured photocurrent density as a function of applied voltage with respect to the reversible hydrogen electrode (RHE). The onset potentials of p-type InP with and without TiO_2 were extracted from the *J–V* plot as 0.81 and 0.63 V *vs.* RHE, respectively. Hence, the TiO_2 passivation increases by almost 200 mV in photocurrent onset potential. This large onset potential provides a large fraction of 1.23 V needed for water splitting in an acidic environment.[23–25] The InP/TiO_2 photocathode has a photocurrent density of 25.2 $mA\,cm^{-2}$, which is similar to 24 $mA\,cm^{-2}$ for bare InP. Lee *et al.* reported a photocurrent density of 37 $mA\,cm^{-2}$ with a p-type InP nanopillar photocathode passivated by 3–5 nm TiO_2 layers in conjunction with a 2 nm Ru co-catalyst.[6] The high photocurrent density is due to enhanced light absorption and less hydrogen gas bubble accumulation resulting from nanotexturing the surface. Figure 5.5b shows chronoamperometry measurements at high positive potentials *vs.* RHE for both samples. Here, the InP/TiO_2 sample shows 19.3 and 9.9 $mA\,cm^{-2}$ at 0.6 and 0.7 V *vs.* RHE, respectively. In contrast, bare InP has a much lower photocurrent density at these applied potentials. In addition, the incident photon-to-charge conversion efficiency (IPCE) was measured in a laboratory-built setup using a 150 W xenon lamp combined with a 1/8 m monochromator. The IPCE for the InP/TiO_2 sample was 70–80% under an applied potential of 0.2 V *vs.* RHE with an incident light wavelength of 400–800 nm, whereas for bare InP only it was less than 30% (Figure 5.5c). The IPCE measurements were conducted under a low illumination intensity in order to study the surface effects of photocathodes, and showed that TiO_2 encapsulation improves the minority carrier extraction capability.

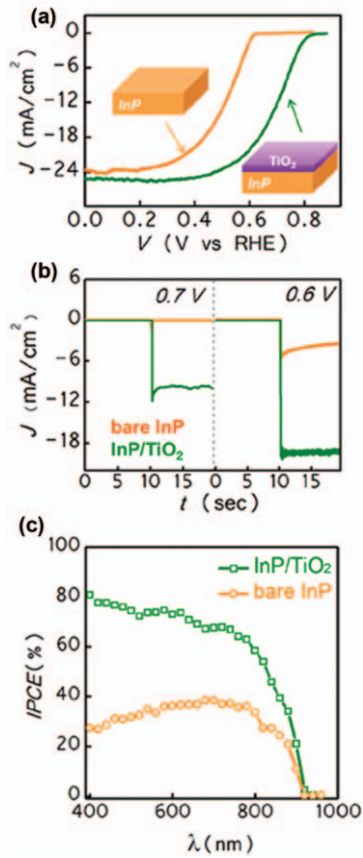

Figure 5.5 (a) Photocurrent density measurements as a function of applied potential *vs.* RHE of InP/TiO_2 (green curve) and bare InP (orange curve). (b) Chronoamperometry measurement of both samples at 0.6 and 0.7 V applied potentials *vs.* RHE with chopped light irradiation. (c) Incident photon-to-charge conversion efficiency (IPCE) of InP/TiO_2 and bare InP with an applied potential of 0.2 V *vs.* RHE in 1 M $HClO_4$ solution. Adapted from ref. 10 with permission from American Chemical Society, Copyright 2015.

In order to obtain carrier concentrations and flat band potentials of p-type InP and n-type TiO_2, Mott–Schottky (MS) measurements were carried out as shown in Figure 5.6a,b. Here, the space charge region capacitance was measured as a function of applied potential *vs.* RHE. A sinusoidal small voltage with 5 mV amplitude and 10 kHz frequency was injected together with DC bias. The carrier concentrations and flat band potentials can be extracted based on the MS equation for a p-type semiconductor:[26,27]

$$\frac{1}{C^2} = \left(\frac{2}{e\varepsilon\varepsilon_0 N_d A^2}\right)\left(-V + V_{fb} - \frac{kT}{e}\right) \tag{5.3}$$

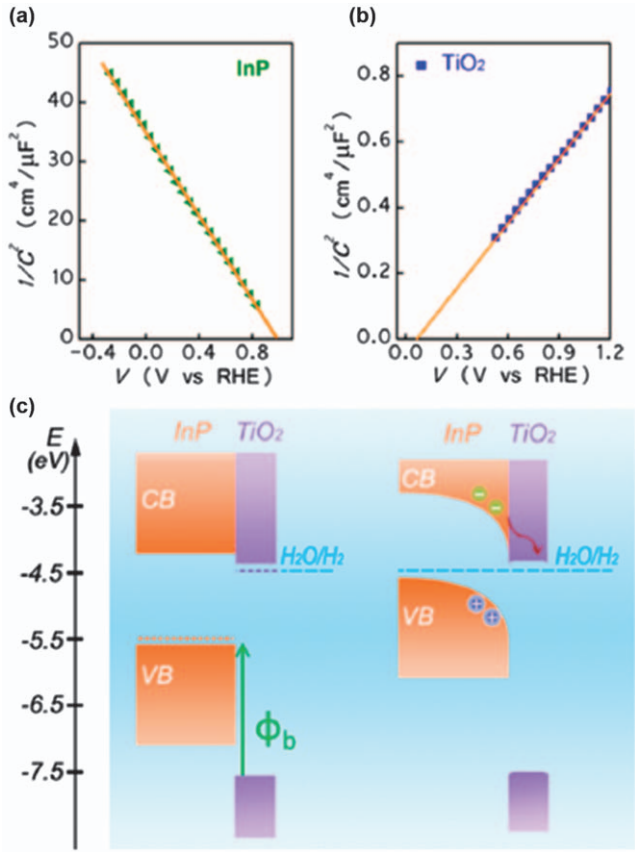

Figure 5.6 Mott–Schottky (MS) plots of (a) p-type InP substrate and (b) 50 nm TiO_2 deposited on an FTO substrate. (c) Band diagram of InP/TiO_2 in 1 M $HClO_4$ solution based on extracted flat band potentials, carrier concentrations and band gaps.
Reprinted with permission from ref. 10 with permission from American Chemical Society, Copyright 2015.

where C is the measured capacitance, e is the electron charge, ε is the dielectric constant, ε_0 is the permittivity of vacuum, N_d is the carrier density, A is the surface area of the photocathode, V is the applied potential *vs.* the reduction potential for the half-reaction of interest (which is RHE for the HER), V_{fb} is the flat band potential, k is the Boltzmann constant, and T is the room temperature. As Figure 5.6a shows, the negative slope of the MS plot indicated p-type doping of the InP substrate, and a carrier density of $3.2\times10^{17}\,cm^{-3}$ was extracted from the slope of linear fitting of the MS curve. A flat band potential of 0.98 V *vs.* RHE of InP was estimated from the x-axis intercept of the linear fitted line. The TiO_2 film grown by ALD and deposited on a fluorine-doped tin oxide (FTO) substrate has a positive slope in MS plot, which indicates n-type doping. A carrier density of about $3.0\times10^{18}\,cm^{-3}$ and a flat band potential of

0.04 V *vs.* RHE were extracted from the linear fitted line in Figure 5.6b. With all these estimated properties combined with the band gap of InP and TiO_2, the energy band diagram of InP/TiO_2/electrolyte can be determined (shown in Figure 5.6c). A type II heterojunction in which two materials form a staggered gap results from a p-type InP substrate and n-type TiO_2 passivation layer, and their conduction band edges are close to each other, thereby assisting transfer of photogenerated electrons from InP to the TiO_2 surface. However, the large offset of the valence band edges between these two layers acts like a blocking layer for holes, leading to lower interface recombination rates. As discussed earlier, this results in a more positive onset potential and higher IPCE for InP/TiO_2 photoelectrodes. For this reason, high performance of the InP/TiO_2 photocathode with a large onset potential and low surface recombination rates was demonstrated. However, the relatively high cost of InP wafers presents a challenge for large-scale commercial application. The approach of using thin films can address the cost problem by reducing the overall material use while keeping all the benefits of InP in photoelectrochemical performance in the HER. Hettick *et al.* demonstrated non-epitaxial growth of thin-film InP on Mo substrates by a vapor–liquid–solid (VLS) method.[15] The as-deposited InP thin film combined with ALD-grown TiO_2 and Pt co-catalyst showed a 29.4 mA cm^{-2} saturated photocurrent density and a 0.63 V *vs.* RHE onset potential, displaying competent performance in the HER compared with single-crystalline InP wafers.

Photoelectrochemical CO_2 reduction in aqueous solution by p-type InP nanopillars encapsulated by an ALD-grown TiO_2 layer was demonstrated by Qiu *et al.*[7] Figure 5.7 shows a schematic diagram together with scanning electron microscopy (SEM) and transmission electron microscopy (TEM) images of a fabricated photocathode. Here, the nanopillars are 80 nm in diameter and 400–600 nm in length with a 250 nm period (shown in Figure 5.7b). A 3 nm thick layer of TiO_2 was coated on the surface of InP nanopillars using $TiCl_4$ and water as precursors. Subsequently, Cu was evaporated onto the TiO_2 surface with a nominal thickness of 0.5 nm. As Figure 5.7d shows, the as-deposited Cu formed nanoparticles with a diameter of ~20 nm rather than a thin continuous film. The surface of the Cu nanoparticles was oxidized to form an amorphous layer of CuO.

Figure 5.8 shows *J–V* measurements of p-type InP nanopillars with and without TiO_2 in 0.5 M KCl aqueous solution with continuous CO_2 bubbling under 532 nm light irradiation. Here, the effect of adding a Cu co-catalyst was excluded in order to study only the role played by the TiO_2 encapsulation layer on the PEC performance. As Figure 5.8a shows, the photocurrent density is dramatically increased with the TiO_2 encapsulation layer compared with bare InP at all applied potentials *vs.* NHE. The onset potential of the InP/TiO_2 sample is 0.1 V higher than that of bare InP nanopillars. The positive shift of the onset potential is attributed to decreased interface recombination rates and a larger built-in potential between the n-type TiO_2 layer and p-type InP nanopillars.[10,28] The NMR spectra in Figure 5.8c show the methanol product peaks using InP nanopillars with and without TiO_2

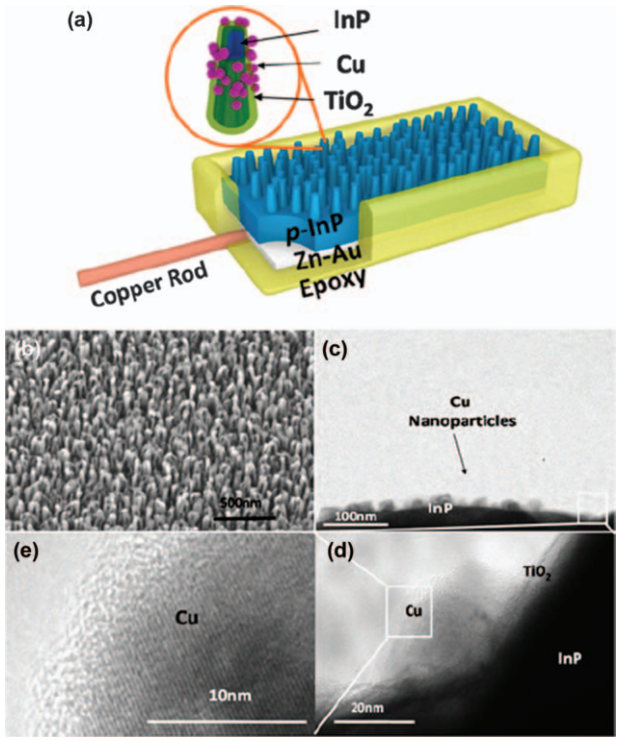

Figure 5.7 (a) Schematic diagram of an as-fabricated InP/TiO_2/Cu photocathode. (b)–(e) SEM and TEM images of InP nanopillars with TiO_2 layers and Cu nanoparticles on the top.
Reproduced from ref. 7 with permission from American Chemical Society, Copyright 2015.

encapsulation as photocathodes at an applied potential of −0.6 V *vs.* NHE under 532 nm irradiation. For CO_2 reduction in aqueous solution under the assumption that CO_2 molecules do not interact with any other molecules in solution or heterogeneous interfaces in the system, the first step of reduction for CO_2 is to form the CO_2^- intermediate, and the redox potential of CO_2/CO_2^- is −1.9 V *vs.* NHE. In the energy diagram, $E^\circ(CO_2/CO_2^-)$ is 1.6 eV above the conduction band edge of InP.[29,30] The applied potential here is −0.6 V *vs.* NHE, which is 1.3 V more positive compared with the CO_2/CO_2^- redox potential (−1.9 V *vs.* NHE). The Faradaic efficiency (FE) describes the efficiency of transferred charge facilitating the target electrochemical reaction, which can be calculated based on the following equation:

$$FE = \frac{nNF}{Q} \times 100\% \tag{5.4}$$

where n is the number of electrons transferred for each product molecule, N is the amount of product in moles in the reaction, F is the Faraday constant,

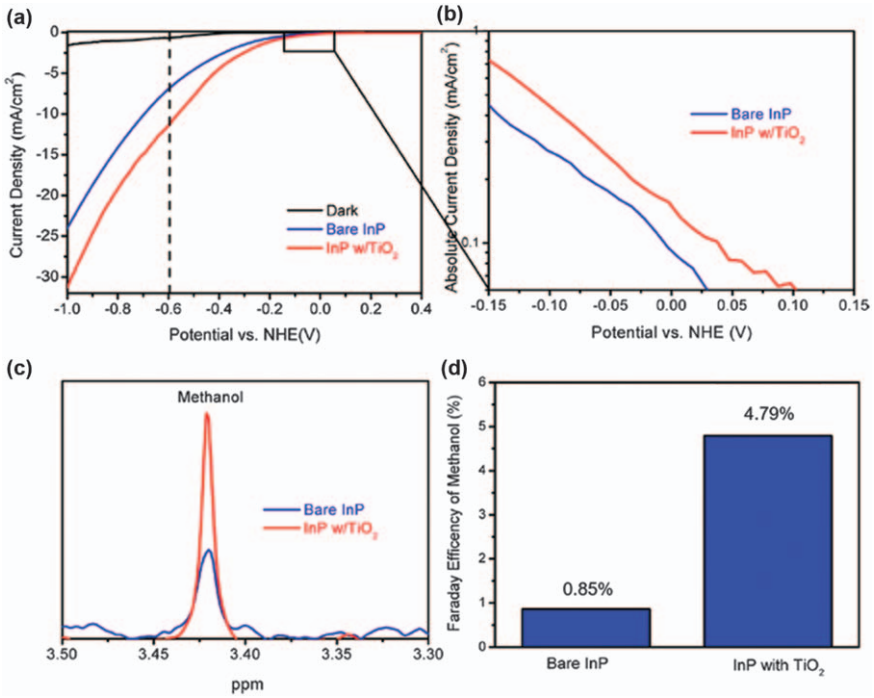

Figure 5.8 (a) Photocurrent density measured as a function of applied potential *vs.* NHE for p-type InP nanopillars with and without TiO_2 passivation under 532 nm monochromatic irradiance in CO_2-saturated 0.5 M KCl solution. The dashed line indicates the potential applied during methanol production. (b) Logarithmic plot of *J–V* measurements near the onset potential region. (c) Methanol peaks in NMR spectra. (d) Faradaic efficiencies of the methanol produced for these two photocathodes.
Reproduced from ref. 7 with permission from American Chemical Society, Copyright 2015.

and *Q* is the total amount of charge passed through. Figure 5.8d shows the FE of methanol production for these two photocathodes, where InP nanopillars with a TiO_2 layer show FE = 4.79%, which is 5.7 times higher than that of bare InP nanopillars. The enhanced FE indicates higher selectivity of the InP/TiO_2 photocathode, which is also attributed to Ti^{3+} defect states. As discussed earlier, the catalytically active Ti^{3+} defect states (*i.e.* oxygen vacancies) substantially lowered the energy required for CO_2 molecules adsorbed on the TiO_2 surface to acquire electrons and form CO_2^- intermediates (Figure 5.3).

In order to study further the selectivity of the Cu co-catalyst on methanol production in PEC CO_2 reduction, a 0.5 nm nominal thickness Cu layer was evaporated onto the surface of as-fabricated photocathodes. As shown in Figure 5.7, the as-deposited Cu formed nanoparticles 20 nm in diameter instead of a continuous thin film. The surface area of the nanoparticles is dramatically increased compared with that of a thin film, which is beneficial

to the PEC reaction. The *J–V* measurements in Figure 5.9a show that the InP/TiO_2/Cu photocathode has the highest photocurrent density at all applied potentials *vs.* NHE. At −0.6 V *vs.* NHE, the photocurrent density of the InP/TiO_2/Cu substrate is around −15 mA cm^{-2}, whereas for bare InP with and without the Cu co-catalyst it is only −7.5 mA cm^{-2}. For bare InP nanopillars, although adding Cu nanoparticles does not change the *J–V* curve profile (Figure 5.9a), the FE is improved from 0.85 to 2.8% for methanol production (Figure 5.9b). In addition, deposition of Cu nanoparticles on the TiO_2 surface enhanced the FE from 4.79% (Figure 5.8d) to 8.7% (Figure 5.9b). These observations clearly demonstrate the selectivity enhancement of Cu nanoparticles towards methanol production over the HER in aqueous solution. In aqueous solution, the HER is always competing with CO_2 reduction, for two reasons. First, the overpotential of the H_2O/H_2 redox reaction is lower than or similar to that of most CO_2 reduction reactions, such as methanol, methane, and carbon monoxide production. Second, the solubility of CO_2 in water is very limited, around 0.033 M at room temperature under 1 atm.[31] The accessibility of CO_2 molecules for these photocathodes is substantially lower than that of water molecules or hydrogen ions. In order to increase further the selectivity of CO_2 reduction over the HER, Zeng *et al.* demonstrated 89% FE towards CO on a 3 nm TiO_2-passivated p-type InP photocathode in CO_2-saturated non-aqueous solution, which consists of 0.02 M 1-ethyl-3-methylimidazolium tetrafluoroborate ([EMIM]BF_4) ionic liquid in acetonitrile.[9] The applied potential is −1.57 V *vs.* NHE and the light source is a 532 nm beam. Here, in addition to photocatalytically active Ti^{3+} defect states, as discussed earlier, an EMIM–CO_2* complex can be formed between [EMIM] ions and CO_2^- intermediates. These complexes can further lower the overpotential associated with the CO_2/CO redox reaction. With the Pt co-catalyst, the FE was further enhanced to 99% towards CO with an applied

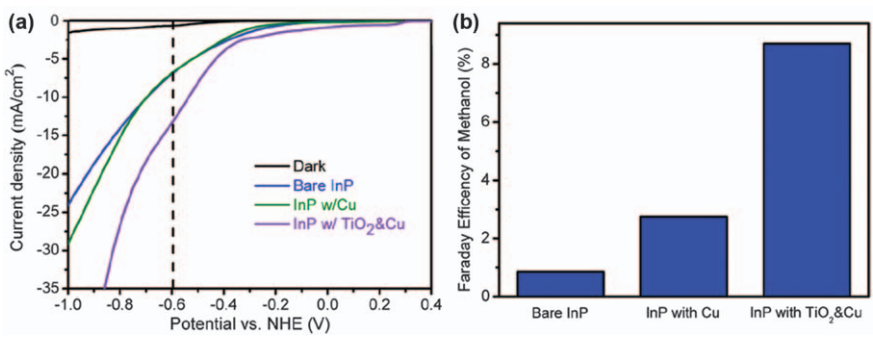

Figure 5.9 (a) *J–V* measurements and (b) Faradaic efficiencies for methanol production with bare InP nanopillars and InP/Cu and InP/TiO_2/Cu photocathodes under 532 nm monochromatic irradiance in CO_2-saturated 0.5 M KCl solution. The dashed line indicates the potential applied during the methanol production experiment.
Reproduced from ref. 7 with permission from American Chemical Society, Copyright 2015.

potential of −0.77 V *vs.* NHE, which showed a 0.78 V underpotential *vs.* the CO_2/CO redox potential (−1.55 V *vs.* NHE).

5.3.2 GaP

GaP is another III–V semiconductor and has a direct band gap of 2.25 eV with more than 18% absorption under solar light. As with InP, it also is not stable during PEC reactions resulting from photocorrosion.[4,32] By introducing a passivating TiO_2 layer on top, the chemical stability of GaP is dramatically increased. In addition, the large valence band offset combined with a built-in electric field between p-type GaP and n-type TiO_2 assists electron extraction while blocking holes.[4] Over the past decade, a new method has emerged for improving the photocatalytic efficiency by utilizing the plasmon resonance of metal nanostructures.[33–38] Since the conduction band energy of GaP is well matched to the resonance energy of Au nanoparticles, adding plasmonic Au nanoparticles can further enhance the photocatalytic performance of the GaP/TiO_2 photocathode.[32] We first discuss the application of GaP as a photocathode in water splitting, followed by a discussion of CO_2 reduction.

Figure 5.10a shows a GaP/TiO_2 photocathode for HER fabricated by Qiu *et al.*[32] Here, a TiO_2 layer grown by ALD at 250 °C was deposited on the surface of Zn-doped p-type GaP with a doping concentration of 2×10^{18} cm^{-3}. $TiCl_4$ and water were used as titanium and oxygen sources, respectively. The photocurrent densities of InP photocathodes with various TiO_2 layer thicknesses were measured as a function of applied potential *vs.* an Ag/AgCl reference electrode in 0.5 M Na_2SO_4 aqueous solution (pH 7) under 532 nm light illumination (shown in Figure 5.10b). RHE = 0 V is also indicated in the *J–V* plot (Figure 5.10b) as a dashed line. Here, the onset potential of the bare GaP photocathode was about −0.66 V *vs.* Ag/AgCl. For TiO_2-passivated GaP samples, the onset potential showed a positive shift with increase in TiO_2 thickness (shown in Figure 5.10c). The onset potential of the sample of GaP with a 10 nm TiO_2 layer shifted by 0.46 V compared with that of the bare GaP substrate. This positive shift is attributed to the increased built-in electric field from the p–n junction between GaP and TiO_2, since GaP is positively doped by Zn and TiO_2 is negatively doped resulting from oxygen vacancies. The built-in potential can be calculated using the following equation:

$$V_{bi} = \frac{W_D^2}{2\varepsilon_0\varepsilon_a\varepsilon_d}\frac{N_a N_d(N_a\varepsilon_a + N_d\varepsilon_d)}{(N_a + N_d)^2} \tag{5.5}$$

where W_D is the depletion width of the p–n junction and increases with increase in TiO_2 thickness, ε_0 is the permittivity of vacuum, ε_a and ε_d are the dielectric constants of GaP and TiO_2, respectively, and N_a and N_d are doping concentrations for GaP and TiO_2, respectively. The calculated built-in potential based on this equation is shown in Figure 5.10c, indicated by dashed line, which exhibited a similar trend to the experimentally measured relative

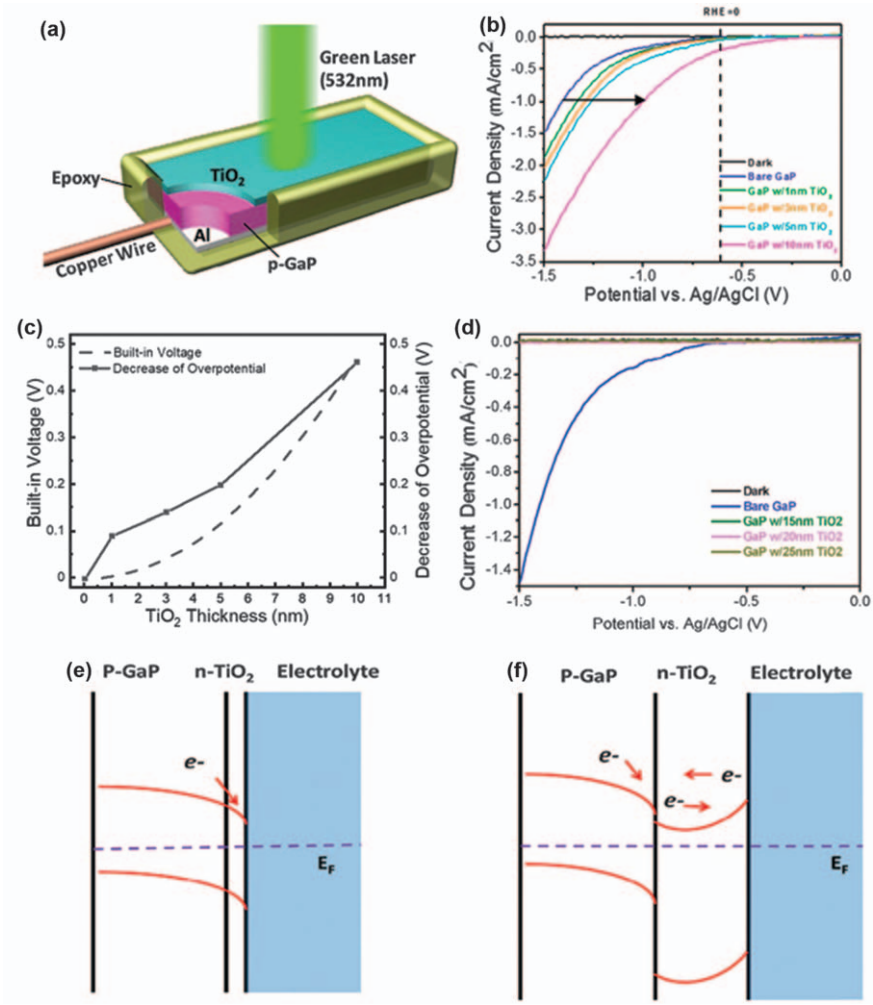

Figure 5.10 (a) Schematic diagram of an as-fabricated GaP/TiO_2 photocathode. (b) Photocurrent densities measured as a function of applied potential *vs.* an Ag/AgCl reference electrode for GaP with different thicknesses of a TiO_2 passivation layer under illumination with 1 W cm^{-2} monochromatic light of wavelength 532 nm in 0.5 M Na_2SO_4 solution (pH 7). The dashed line indicates RHE = 0 V. (c) Measured relative shift of onset potentials (solid line) and calculated built-in electric field (dashed line) with respect to TiO_2 thickness. (d) *J–V* measurement of GaP samples with thicker TiO_2 passivation layers. Band diagrams of GaP photocathode with (e) thin and (f) thick TiO_2 layers.
Adapted from ref. 32 with permission from the Royal Society of Chemistry.

positive shift of the onset potential of TiO_2-passivated GaP with respect to bare GaP (solid line in Figure 5.10c). The band diagrams of the GaP/TiO_2/electrolyte with thin and thick TiO_2 layers are shown in Figure 5.10e,f. The

downward band bending of p-type GaP at the GaP/TiO_2 interface will facilitate photogenerated electron transfer towards the electrolyte, while the upward band bending of n-type TiO_2 at the TiO_2/electrolyte interface prevents the electron transfer from TiO_2 to water adsorbates. Therefore, it is surprising to observe that GaP/TiO_2 still functions as a photocathode with a 10 nm thick TiO_2 passivation layer. This is due to the complete depletion of the TiO_2 layer when the layer is relatively thin. However, when the TiO_2 thickness increased to 15 nm, the photocurrent density decreased dramatically to near zero at all measured applied potentials *vs.* an Ag/AgCl electrode, as shown in Figure 5.10d.

The effect of plasmonic Au nanoparticles on the photocatalytic performance of GaP/TiO_2 photocathodes was also studied (Figure 5.11).[32] Here, a 5 nm nominal thickness of Au was evaporated onto the as-fabricated photocathodes. An island-like morphology was formed with this deposition and the gaps between islands were about 2–3 nm in length. The electric fields

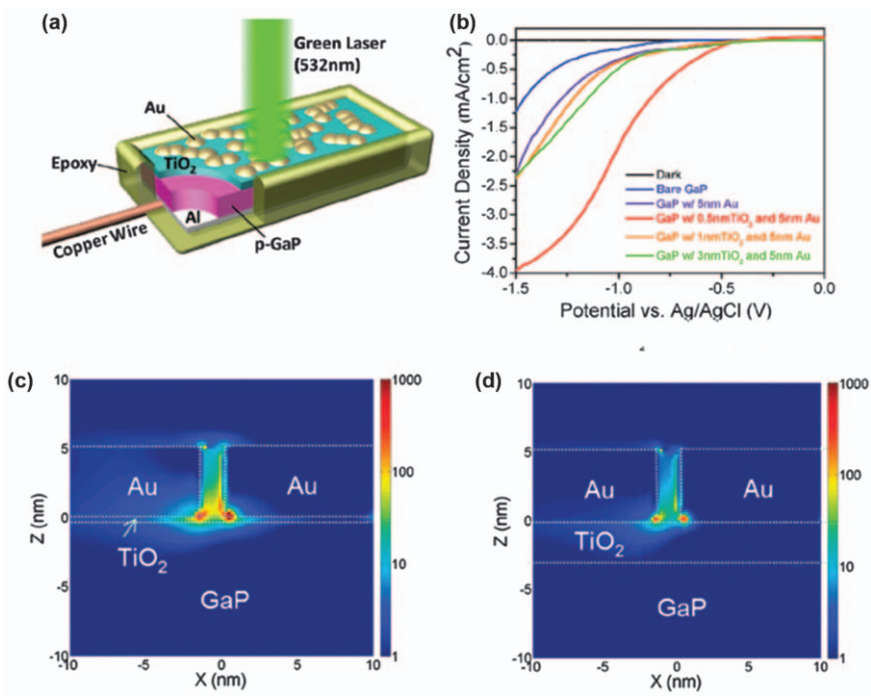

Figure 5.11 (a) Schematic illustration of the GaP/TiO_2/Au photocathode geometry. (b) Photocurrent densities measured with respect to applied voltage *vs.* an Ag/AgCl reference electrode under illumination with 1 W cm^{-2} monochromatic light of wavelength 532 nm in 0.5 M Na_2SO_4 solution. Simulated electric field distributions in the cross-section of the photocathode/electrolyte interface for (c) a 0.5 nm and (d) a 3 nm TiO_2 passivation layer.
Reproduced from ref. 32 with permission from the Royal Society of Chemistry.

were highly concentrated at the edges of Au islands near these nanogaps, which was also validated by surface-enhanced Raman spectroscopy and photocatalytic measurements in other materials.[39–44] Figure 5.11b shows *J–V* measurements of GaP/TiO_2 photocathodes decorated with 5 nm Au nanoparticles under illumination with 1 W cm^{-2} monochromatic light of wavelength 532 nm in 0.5 M Na_2SO_4 solution for the HER. The GaP/Au with TiO_2 encapsulation showed better performance than bare GaP, exhibiting a 0.2 V positive shift of the HER onset potential. Furthermore, Au evaporation made GaP/TiO_2 photocathodes perform even better, where samples with a 0.5 nm TiO_2 layer showed the highest photocurrent density at all measured potentials *vs.* Ag/AgCl, with a fourfold enhancement with respect to a bare GaP substrate at −0.7 V *vs.* Ag/AgCl. This behavior results from the trade-off between the localized concentrated electric fields due to the plasmonic effect and built-in p–n junction potential. Figure 5.11c shows the calculated electric field distribution for one Au nanogap at the photocathode/electrolyte interface with a 0.5 nm TiO_2 passivation layer using the finite difference time domain (FDTD) method. Here, a 1000-fold enhancement factor is observed for the electric field intensity near the nanogap with respect to that of the incident light. The enhancement of photocatalytic performance by the plasmonic effect is due to three reasons. First, the highly concentrated electric field promotes the generation of more electron–hole pairs near the photocathode/electrolyte interface and charge separation region. Second, the increased intensity of light at the heterojunction produces a higher open-circuit voltage, leading to a more positive shift of the onset potential for the HER. Third, hot electrons generated from plasmon resonance decay from Au nanoparticles may participate directly in the HER.[33,34,45–47] Hence the photocatalytic performance of GaP is greatly enhanced by TiO_2 encapsulation combined with plasmonic Au nanoparticles.

The application of p-type GaP in photocatalytic CO_2 reduction was demonstrated by Zeng *et al.*[4] Figure 5.12a shows *J–V* measurements for GaP with various thicknesses of a TiO_2 layer (up to 10 nm) in CO_2-saturated aqueous solution consisting of 0.5 M NaCl and 10 mM pyridine under 532 nm light irradiation. The addition of pyridine increases the selectivity for CO_2 to be reduced to methanol through a series of steps involving one-electron transfer at low overpotentials.[48,49] A bare p-type GaP photocathode shows an onset potential of −0.15 V *vs.* NHE. For GaP samples passivated with a TiO_2 layer, a clear positive shift of the onset potential was observed that increased with increase in the TiO_2 layer thickness (Figure 5.12b). For GaP with a 10 nm TiO_2 layer, the onset potential shifted by 0.52 V compared with that of bare GaP. This positive shift is attributed, first, to the built-in potential between p-type GaP and n-type TiO_2. Under the assumption of complete depletion of thin TiO_2 layers, the built-in potential also increases as the thickness of the TiO_2 layer increases. We can calculate this potential based on eqn (5.5) as discussed earlier. Figure 5.12c shows the calculated built-in voltage as a function of TiO_2 thickness, and reveals a similar trend to the experimentally measured overpotential decrease in Figure 5.12b. In addition, the large valence band

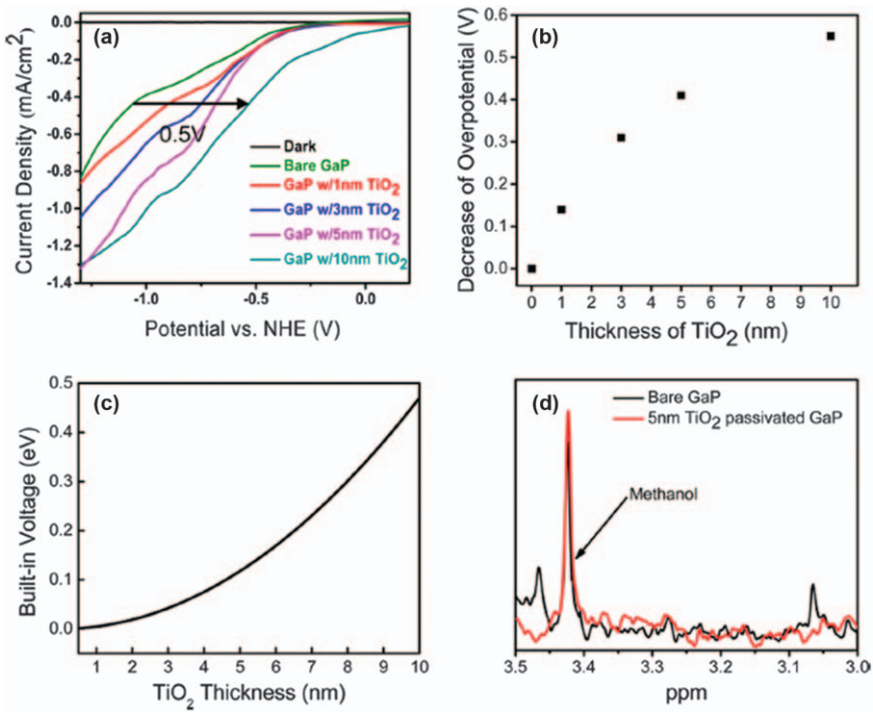

Figure 5.12 (a) Photocurrent densities measured as a function of applied potential *vs.* NHE for GaP photocathodes with different thicknesses of a TiO_2 layer in CO_2-saturated aqueous solution consisting of 0.5 M NaCl and 10 mM pyridine under 532 nm illumination. (b) Decrease in overpotential plotted against TiO_2 thickness. (c) Built-in voltage of GaP/TiO_2 p–n junction calculated as a function of TiO_2 thickness. (d) NMR spectra for bare GaP and GaP with a 5 nm TiO_2 layer at an applied potential of −0.5 V *vs.* NHE.
Reproduced from ref. 4 with permission from American Chemical Society, Copyright 2014.

offset between TiO_2 and GaP makes the interface act like a hole-blocking layer, leading to decreased recombination rates. However, when the TiO_2 thickness is >10 nm, no enhancement in photocurrent is observed. This is due to band bending between n-type TiO_2 and the electrolyte that will block electrons from entering the electrolyte and participate in reduction reactions. In addition, TiO_2 will change from a conducting amorphous structure to an insulating crystalline structure when it is thicker than 10 nm. Furthermore, when the TiO_2 layer is thin and less than 10 nm, photogenerated electrons inside GaP can travel ballistically without equilibrating to the conduction band edge of TiO_2.[4] However, as the TiO_2 layer becomes thicker and reaches >10 nm, the electrons will travel diffusively and need a higher overpotential to participate in the reaction because the conduction band of GaP has a higher conduction band energy than that of TiO_2.

Figure 5.12d shows the NMR spectra of the electrolyte after operating GaP photocathodes with and without TiO_2 for 8 h under an applied potential of −0.5 V *vs.* NHE under illumination for 8 h with 532 nm monochromatic light. Here, the measured data clearly show the methanol peak for both samples. However, the bare GaP photocathode shows severe photocorrosion on the surface whereas the TiO_2-encapsulated GaP is still stable after the measurement. The FE for GaP with a 5 nm TiO_2 layer is about 55%. In order to eliminate the possibility of other carbon sources in the solution, isotopically labeled $^{13}CO_2$ was used in the reaction and the $^{13}CH_3OH$ peak was observed in the NMR spectra. In addition, when Ar was bubbled through the solution instead of CO_2, no methanol was detected in the NMR characterization. Hence CO_2 is indeed the carbon source for this reduction reaction. When pyridine was not added to the solution, the methanol peak could still be detected, but the yield decreased by two-thirds. This is because pyridine catalysts help lower the energy barrier of CO_2 reduction through inner-sphere type electron transfer.[50] In conclusion, TiO_2 passivation not only stabilized the GaP surface, but also enhanced its photocatalytic performance, and adding pyridine further increased the selectivity for methanol production.

5.3.3 GaAs

GaAs is a direct band gap semiconductor with a band gap energy of 1.42 eV, which makes it a good light absorber under solar illumination. However, the surface recombination velocity of GaAs is about 10^6 cm s^{-1}, which is higher than those of most other III–V compound semiconductors by 1–2 orders of magnitude, thereby lowering its efficiency in photocatalytic applications.[51,52] The surface of GaAs also lacks stability and changes color during the photocatalysis. By depositing a thin layer of TiO_2 on the surface, the dangling bonds will be passivated, leading to decreased surface recombination rates. The stability issue is also minimized by TiO_2 passivation.[8,13]

Figure 5.13a shows a schematic illustration of a p-type GaAs photocathode encapsulated by TiO_2 fabricated by Qiu *et al.*[13] A Ti–Au film was evaporated onto the back side of the GaAs to form an ohmic contact. TiO_2 was deposited by ALD at 250 °C with $TiCl_4$ as the titanium source and water as oxygen source. Figure 13b shows a cross-sectional HRTEM image of GaAs with a 3 nm TiO_2 layer. Here, TiO_2 forms an amorphous structure instead of a crystalline anatase structure. As discussed earlier, amorphous TiO_2 has a better conducting ability than crystalline films, thus showing better photocatalytic ability. Pt was deposited here only for the purpose of TEM imaging and was not used in the photoelectrochemical measurement. The photocurrent densities were measured with respect to the applied potential *vs.* RHE in 0.5 M H_2SO_4 aqueous solution (pH 0) under AM1.5 illumination to drive the hydrogen evolution half-reaction (Figure 5.13c). Here, the onset potential of bare GaAs is about −0.05 V *vs.* RHE. Upon TiO_2 passivation, there is a clear positive shift in onset potential for GaAs photocathodes with a passivation layer up to 5 nm thick. Among them, GaAs with a 1 nm TiO_2

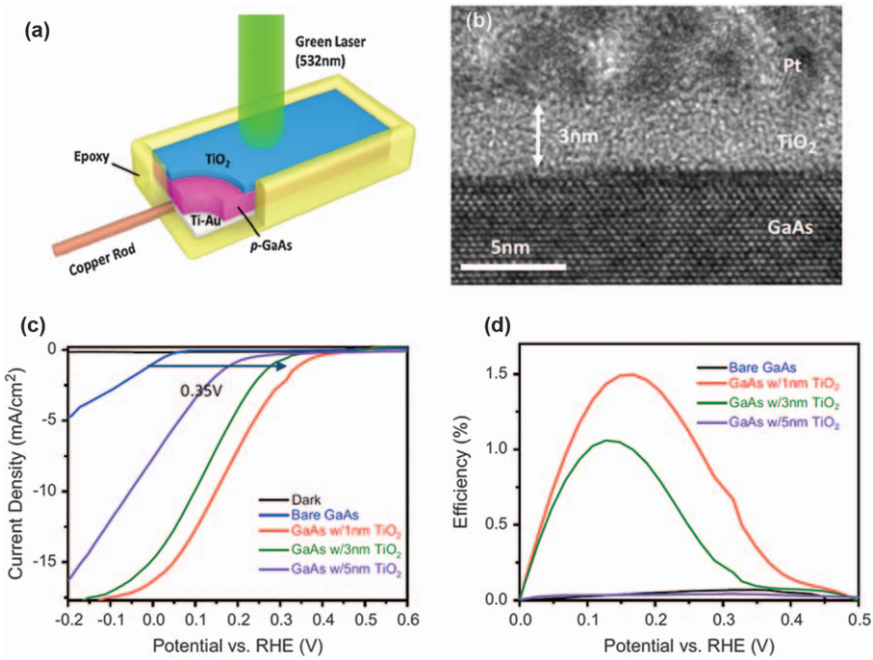

Figure 5.13 (a) Schematic illustration of a TiO_2-passivated p-type GaAs photocathode. (b) HRTEM image of GaAs with a 3 nm TiO_2 layer. (c) *J–V* measurements and (d) calculated ABPE based on eqn (5.2) for GaAs photocathodes with different thicknesses of the TiO_2 layer in 0.5 M H_2SO_4 aqueous solution under AM1.5 illumination.
Reproduced from ref. 13 with permission from Elsevier, Copyright 2016.

layer shows the largest shift of 0.35 V at 1 mA cm^{-2} compared with bare GaAs, which is indicated in the *J–V* plot. At an applied potential of 0 V *vs.* RHE, the photocurrent density of GaAs with a 1 nm TiO_2 layer increases by a factor of 32 with respect to that of bare GaAs.

Figure 5.13d shows the estimated ABPE for GaAs encapsulated with various thicknesses of TiO_2 together with a bare GaAs photocathode. GaAs with a 1 nm TiO_2 layer shows the highest efficiency of 1.5% when the applied potential is 0.2 V *vs.* RHE. It should be noted that no co-catalyst was added in the study. The purpose of the study was to analyze the effect of TiO_2 rather than to achieve the best performance. The reason why 1 nm TiO_2-encapsulated GaAs shows the highest onset potential and hydrogen conversion efficiency is that it has the highest concentration of defect states. As discussed earlier, the XPS spectra (Figure 5.4a) show the highest area ratio of Ti^{3+} to Ti $2p_{1/2}$ for a 1 nm TiO_2 layer. In addition, the area ratio between Ob and Oa is also highest for a 1 nm TiO_2 film (Figure 5.4b), and Ob is associated with oxygen vacancies. As the TiO_2 thickness is increased to more than 10 nm, the photocatalytic ability of the GaAs/TiO_2 photocathode is dramatically

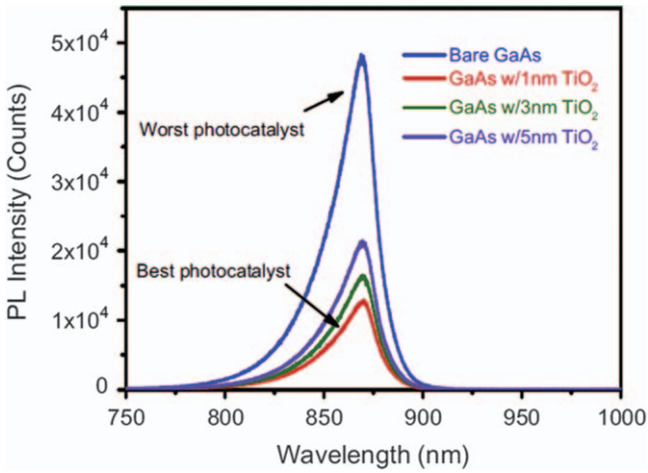

Figure 5.14 PL spectra of p-type GaAs photocatalysts with different thicknesses of TiO_2 encapsulation layer under 532 nm irradiation. Reproduced from ref. 13 with permission from Elsevier, Copyright 2016.

suppressed. This is due to the transfer from a thin amorphous conducting phase to a thick crystalline insulating phase (Figure 5.2). Qiu *et al.* also studied CO_2 reduction using GaAs/TiO_2 and found a similar trend.[8]

Photoluminescence (PL) spectroscopy has been used to explore further the role of TiO_2 encapsulation in electron–hole recombination process within GaAs photocathodes. Figure 5.14 shows the PL spectra for different thicknesses of TiO_2 layers on GaAs surfaces.[13] Here, samples with the lowest PL efficiency showed the highest photocatalytic performance, and *vice versa*. GaAs with a 1 nm TiO_2 layer has a fivefold lower PL intensity compared with bare GaAs but demonstrates the best photocatalytic performance in the HER in 0.5 M H_2SO_4 solution. This finding was initially surprising because materials with strong PL intensity typically tend to show high performance in solar cells and photocatalytic applications. However, the Ti^{3+} surface states described above can also cause additional electron–hole recombination, thus lowering the PL intensity and shortening photoexcited carrier lifetimes. However, the benefits of surface states in lowering the reaction potential barrier and promoting electrochemical charge transfer at the TiO_2/electrolyte interface outweigh their roles as non-radiative recombination centers.

5.4 pH and Electrode Potential Stability Range

5.4.1 Pourbaix Diagram of Titanium

In order to further study the stability of TiO_2 under various applied potentials and pH values, a Pourbaix diagram of titanium is worth considering. Marcel Pourbaix first proposed using an electrode potential–pH equilibrium diagram

to summarize the corrosion conditions of a given metal, where the *y*-axis is the applied potential, typically plotted with respect the standard hydrogen electrode (SHE), and the *x*-axis is the pH value of the aqueous environment.[53] Pourbaix diagrams are constructed using thermodynamic principles under the assumption that the metal reaches an equilibrium with its environment.[54] Figure 5.15 shows the Pourbaix diagram of the Ti–H_2O system, in which each region in the diagram indicates the most thermodynamically stable titanium chemical compound. If the most stable chemical compound in the region is the metal itself, it is labeled *immunity*. If the dissolved ion is the most stable species, then it is labeled *corrosion*. If the metal oxide is the most stable in that region, the label *passivation* is used in Figure 5.15.

There are three different kinds of boundary lines between each region within the Pourbaix diagram. The horizontal lines indicate the reactions involved that depend only on the applied potential and not on the pH value. For example, the boundary line between the Ti and Ti^{2+} region is horizontal, and the reaction involved is the following:

$$Ti^{2+} + 2e^- \rightarrow Ti \tag{5.6}$$

This an electrochemical reaction and does not involve protons or hydroxide ions. The reduction potential *E vs.* SHE can be calculated using the Nernst equation:

$$E = E^0 - (2.303RT/nF)\log(1/[Ti^{2+}]) \tag{5.7}$$

where E° is the standard reduction potential of the Ti^{2+}/Ti reaction, R is the ideal gas constant, T is the absolute temperature, n is the number of electrons transferred in the reaction equation, F is the Faraday constant and

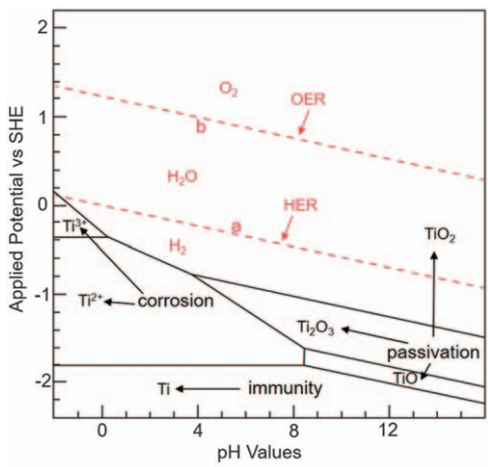

Figure 5.15 Pourbaix diagram for titanium at 25 °C.

$[Ti^{2+}]$ is the concentration of Ti^{2+}. Based on $E^{\circ} = -1.63$ V *vs.* SHE and $n = 2$, eqn (5.7) can be rewritten as

$$E = -1.63 + 0.0296 \log [Ti^{2+}] \tag{5.8}$$

As eqn (5.8) shows, the reduction potential is a function of Ti^{2+} concentration. Conventionally, a minimum concentration of Ti^{2+} of 1.0×10^{-6} M provides the condition for Ti to be corroded in the Pourbaix diagram construction. Putting this into eqn (5.7) gives a reduction potential of $E = -1.81$ V *vs.* SHE for the Ti^{2+}–Ti reaction, as shown in Figure 5.15. When the applied potential is more negative than -1.81 V, the concentration of Ti^{2+} is lower than 1.0×10^{-6} M, and the most stable species is then Ti metal. We say that Ti is *immune* under this condition, as labeled in Figure 5.15. In contrast, when the applied potential is more positive than -1.81 V *vs.* SHE, the Ti^{2+} concentration is higher than 1.0×10^{-6} M, and Ti therefore undergoes corrosion and Ti^{2+} becomes the most stable species.

The second type of boundary lines in the Pourbaix diagram is vertical. These only involve changes in pH values and chemical reactions that do not require electron transfer. Consequently, the applied potential does not affect the reaction in this category. For example, the Ti^{2+}–TiO reaction proceeds as follows:

$$Ti^{2+} + H_2O \rightarrow TiO + 2H^+ \tag{5.9}$$

Based on the standard Gibbs free energy change:

$$\Delta G^{\circ} = -2.303RT \log K \tag{5.10}$$

where ΔG° is the standard Gibbs free energy change and K is the equilibrium constant, for eqn (5.9) $\Delta G^{\circ} = 14\,870$ cal mol^{-1} and

$$K = \frac{[H^+]^2}{[Ti^{2+}]} \tag{5.11}$$

Combining eqn (5.10) and (5.11) yields

$$14870 \text{ cal mol}^{-1} = -2.303(1.98 \text{ cal mol}^{-1} \text{ K}^1)(298 \text{ K}) \log([H^+]^2/[Ti^{2+}]) \tag{5.12}$$

which can be reduced to

$$\log[Ti^{2+}] = 10.94 - 2\text{pH} \tag{5.13}$$

If we use a Ti^{2+} concentration of 1.0×10^{-6} M as the minimum value, the calculated pH value will be 8.47. Therefore, when the pH value is higher than 8.47, the Ti^{2+} concentration is lower than 1.0×10^{-6} M, causing TiO to be the most stable species. This region is called *passivation* since the metal oxide has the highest stability. On the other hand, when the pH value drops below

8.47, the concentration of Ti^{2+} is higher than 1.0×10^{-6} M, causing corrosion on the metal surface, as shown in Figure 5.15.

The third kind of reactions not only depend on the applied potential but are also affected by the pH value. The associated boundary lines are shown to be slanted in the Pourbaix diagram. For the Ti^{2+}–TiO_2 reaction:

$$Ti^{2+} + 2H_2O \rightarrow TiO_2 + 4H^+ + 2e^- \tag{5.14}$$

the Nernst equation gives

$$E = E^0 - (2.303RT/nF)\log([H^+]^4/[Ti^{2+}]) \tag{5.15}$$

For anhydrous TiO_2, eqn (5.15) can be reduced to

$$E = -0.502 - 0.1184\text{pH} - 0.0296\ \log[Ti^{2+}] \tag{5.16}$$

Using the concentration of 1.0×10^{-6} M as the minimum value, we can draw this potential–pH line associated with the Ti^{2+}–TiO_2 reaction in the Pourbaix diagram, and the stability regions can also be labeled based on the same discussion as used previously. All the stability regions can be drawn using this method. One convenient aspect of the Pourbaix diagrams is that the two independent parameters (applied potential and pH value) are chosen such that the boundary lines between different stable regions are always linear. That is to say, a given pH value is chosen to linearize the equilibrium relations with applied potential. Therefore, in the Pourbaix diagram, the 2D potential–pH plane is divided into various regions of stability by straight lines.

The dashed line labeled "a" in Figure 5.15 is associated with the HER. As we know, in acidic solution, the HER is

$$2H^+ + 2e^- \rightarrow H_2 \tag{5.17}$$

The Nernst equation for this reaction at 25 °C and 1 atm of H_2 is

$$E = 0 - (2.303RT/nF)\log(1/[H^+]^2\| - 0.0591\text{pH} \tag{5.18}$$

In basic solution, the HER is

$$2H_2O + 2e^- \rightarrow H_2 + 2OH^- \tag{5.19}$$

and the Nernst equation is

$$E = -0.83 - \frac{2.303RT}{nF}\log[OH^-]^2 = -0.0591\text{pH} \tag{5.20}$$

Whereas the HER originates from different reactions in acidic and basic solutions, the Nernst equation has the same final expression and depends only on the pH of the solution. The dashed line "a" in Figure 5.15 is drawn

based on this equation. At a certain pH value, when the applied potential is below −0.0591pH, the HER is driven and H_2 is the most stable chemical compound. When the applied potential is above this value, the water molecule or proton is the most stable species.

The line labeled "b" in Figure 5.15 corresponds to the oxygen evolution reaction (OER):

$$2H_2O \rightarrow O_2 + 4H^+ + 4e^- \tag{5.21}$$

The associated Nernst equation at 25 °C and 1 atm of O_2 is

$$E = 1.23 - 0.0591\text{pH} \tag{5.22}$$

Above this potential at a given pH value, the OER is driven forwards and O_2 is the most stable species. Below this potential, the water molecule is stable. Therefore, when the applied potential is between the "a" and "b" lines, water is stable. In addition, the HER is driven below the "a" line and the OER is driven above the "b" line.

Based on the Pourbaix diagram of the Ti–H_2O system plotted in Figure 5.15, we note that titanium is expected to be passivated by its oxides when driving the HER over a wide range of pH values and at moderate HER overpotentials. It is for this reason that TiO_2 passivation on III–V semiconductors is indeed a good strategy for preventing photocorrosion in the HER. For CO_2 reduction reactions, it is much more complicated because the CO_2 molecules can be reduced to many different products in the same electrochemical or photoelectrochemical experiment, such as methanol, carbon monoxide, methane, and formic acid.[55] When driving the reduction reaction associated with each product, titanium may be in the *corrosion* region based on the Pourbaix diagram and not able to protect the underlying photocathode. Even if we can draw the lines associated with different CO_2 reduction reactions on the Pourbaix diagram, under certain applied potentials and pH values, when titanium is in the *immunity* or *passivation* region, activation energy barriers may be too high such that the reaction rate for producing this product is low. This leads to the production of less thermodynamically stable products with low activation energy barriers. Improving the selectivity of CO_2 reduction catalysts is an active area of research.

5.4.2 Limits of Pourbaix Diagrams

Several aspects must be considered when using Pourbaix diagrams to predict the most stable chemical compounds for a metal in an aqueous environment. The chemical behavior of the metal or metal oxide in the electrolyte mostly depends on the composition of the layer that is in immediate contact with the electrolytic medium. This topmost or surface layer may be amorphous rather than crystalline and tends to be hydrated. As discussed previously, Qiu *et al.* showed that a 1 nm TiO_2-passivated p-type GaAs photocathode exhibits the most positive shift of onset potential, and a 1 nm TiO_2 layer shows an amorphous structure under TEM imaging.[8] Although both amorphous and

crystalline TiO_2 can provide protection, the amorphous form is more conducting, thus exhibiting a higher photocurrent density at the same applied potential. In addition, the chemical behavior also depends on the composition of the solution layer near the interfaces. When considering ion migration and diffusion at the interface between the solution and metallic phases, the composition of the solution phase near the interface may differ dramatically from the initial or mean composition of the electrolyte. For this reason, certain corrections must be made when using Pourbaix diagrams, such as for the deviation of the real solid or liquid phase from the ideal form.[54]

Since the Pourbaix diagrams are constructed based on thermodynamic principles, no information about the reaction rates is provided. For a certain metal, it may be in the *passivation* region under some applied potential and pH value through forming a surface oxide or hydroxide layer, and the rate of formation of the passivation layer may be very slow such that pure metallic phase is still exposed to the electrolyte, leading to more corrosion. On the other hand, even if the passivation layer forms rapidly, it may not be sufficient to reduce the rate of the corrosion reaction between the underlying metal and the electrolyte below the tolerable limit. Therefore, the corrosion may still proceed by ion diffusion through the passivation layer, which is also ignored in the Pourbaix diagram. To study the reaction mechanism and associated intermediates, surface Pourbaix diagrams are indispensable. Li *et al.* investigated the proton–electron interplay at the interface between rutile TiO_2 and electrolyte to construct surface Pourbaix diagrams for the water oxidation reaction.[56] In their study, different surface Pourbaix diagrams were simulated using different values of the Helmholtz layer capacitance and TiO_2 doping level.

5.5 Outlook

Although the chemical stability and PEC performance of III–V compound semiconductors are greatly improved by TiO_2 encapsulation, several other strategies are currently under exploration for further enhancement. One of these is to nanostructure the TiO_2 layer to provide various waveguide modes for incident light coupling.[57–59] Since efficient photoelectrodes require catalysts to decrease the overpotentials of target reactions, those catalysts make the light-facing surface more opaque, thus reducing the amount of light absorbed by underlying photoelectrodes. Yalamanchili *et al.* demonstrated high broadband light transmission on TiO_2 nanocones decorated on a p^+–n Si photoanode with Ni as the catalyst for the OER.[59] Based on their FDTD simulation, these nanocones serve both as a protection and an anti-reflection layer that allows >85% transmission of broadband light although they only cover less than 50% of the total Si surface with a 50 nm thick Ni layer covering the remainder of the surface. The fabricated photoanode shows saturation at a photocurrent density of 28 $mA\,cm^{-2}$ under 100 $mW\,cm^{-2}$ AM1.5 solar illumination in 1.0 M KOH aqueous solution for the OER.

It is difficult for a single III–V compound semiconductor to generate enough photovoltage to overcome overpotential losses and split water autonomously (*i.e.* without an externally applied voltage). However, semiconductors can be combined to form a multijunction tandem cell for unassisted water splitting.[60–63] Khaselev and Turner demonstrated unassisted water splitting based on a monolithic PEC–photovoltaic device with a solar-to-hydrogen conversion (STH) efficiency of 12.4% under 11 sun illumination in 3 M H_2SO_4 solution.[60] In their device, p-$GaInP_2$ serves as the top cell for the HER, which is connected to a p–n GaAs bottom cell through a tunneling diode interconnect, and a Pt counter electrode is wired to the bottom cell to drive the OER. However, this device suffered localized damage without a surface protection layer. Later, Verlage *et al.* showed stable unassisted water splitting performances for over 40 h of operation with an STH efficiency of >10% on a monolithically TiO_2-protected device under AM1.5 solar illumination in 1 M KOH solution. The as-fabricated device consists of GaAs/$InGaP_2$/TiO_2/Ni as the photoanode to drive the OER, which is connected to an Ni–Mo-coated counter electrode for the HER.[61] They also showcased a fully integrated wireless device based on an NiMo/GaAs/$InGaP_2$/TiO_2/Ni structure conducting the HER and OER on each side. This membrane-based prototype showed an STH efficiency of 8.6% under AM1.5 solar illumination in 1 M KOH solution with separate collection of H_2 and O_2 streams.

In addition to TiO_2, other metal oxide protection layers are also being studied for III–V compound semiconductors in PEC applications. Sun *et al.* showed that sputtered NiO_x film can also be used to protect p^+–n InP photoanodes in the OER under AM1.5 illumination in 1.0 M KOH aqueous solution.[64] In addition to protection, the as-sputtered conductive NiO_x film also serves as the catalyst and anti-reflective layer. Based on the Pourbaix diagram, tantalum is also very resistant to corrosion and has larger regions of passivation and immunity than titanium.[53,54] The passivation of Ta_2O_5 on III–V semiconductors for photoelectrochemical applications is also an active topic of research that holds much promise for future photocatalytic systems.

In conclusion, this chapter has discussed the benefits of n-type TiO_2 passivation on p-type III–V semiconductors for photocatalytic applications, including chemical stability, large valence band offset, built-in potential, and surface defect states. The effects of nanotexturing, co-catalysts, and plasmonic nanoparticles on the photocatalytic performance for those III–V semiconductors were also discussed. Three types of factors, thermodynamic principles, kinetics, and phase equilibria structures, must all be considered when evaluating the electrochemical stability of TiO_2-passivated photocathodes. When combined with kinetic and structural analysis, the Pourbaix diagrams provide a powerful tool in understanding the corrosion conditions for metals in practical experiments and energy conversion applications. Future research efforts will probably be focused on nanostructuring protective oxide layer films, combining different III–V semiconductors for unassisted water splitting, and exploring other metal oxide protection layers in PEC applications.

Acknowledgements

This research was supported by the Air Force Office of Scientific Research (AFOSR) grant No. FA9550-19-1-0115 (Y.W.) and the Department of Energy (DOE) award No. DE-SC0019322 (S.B.C.).

References

1. A. Fujishima and K. Honda, *Nature*, 1972, **238**, 37–38.
2. W. Shockley and H. J. Queisser, *J. Appl. Phys.*, 1961, **32**, 510–519.
3. C. Liu, N. P. Dasgupta and P. Yang, *Chem. Mater.*, 2014, **26**, 415–422.
4. G. Zeng, J. Qiu, Z. Li, P. Pavaskar and S. B. Cronin, *ACS Catal.*, 2014, **4**, 3512–3516.
5. Y. W. Chen, J. D. Prange, S. Dühnen, Y. Park, M. Gunji, C. E. D. Chidsey and P. C. McIntyre, *Nat. Mater.*, 2011, **10**, 539–544.
6. M. H. Lee, K. Takei, J. Zhang, R. Kapadia, M. Zheng, Y.-Z. Chen, J. Nah, T. S. Matthews, Y.-L. Chueh, J. W. Ager and A. Javey, *Angew. Chem., Int. Ed.*, 2012, **51**, 10760–10764.
7. J. Qiu, G. Zeng, M.-A. Ha, M. Ge, Y. Lin, M. Hettick, B. Hou, A. N. Alexandrova, A. Javey and S. B. Cronin, *Nano Lett.*, 2015, **15**, 6177–6181.
8. J. Qiu, G. Zeng, M.-A. Ha, B. Hou, M. Mecklenburg, H. Shi, A. N. Alexandrova and S. B. Cronin, *Chem. Mater.*, 2015, **27**, 7977–7981.
9. G. Zeng, J. Qiu, B. Hou, H. Shi, Y. Lin, M. Hettick, A. Javey and S. B. Cronin, *Chem. – Eur. J.*, 2015, **21**, 13502–13507.
10. Y. Lin, R. Kapadia, J. Yang, M. Zheng, K. Chen, M. Hettick, X. Yin, C. Battaglia, I. D. Sharp, J. W. Ager and A. Javey, *J. Phys. Chem. C*, 2015, **119**, 2308–2313.
11. R. W. Johnson, A. Hultqvist and S. F. Bent, *Mater. Today*, 2014, **17**, 236–246.
12. J.-P. Niemelä, G. Marin and M. Karppinen, *Semicond. Sci. Technol.*, 2017, **32**, 093005.
13. J. Qiu, G. Zeng, M. Ge, S. Arab, M. Mecklenburg, B. Hou, C. Shen, A. V. Benderskii and S. B. Cronin, *J. Catal.*, 2016, **337**, 133–137.
14. A. G. Scheuermann, J. D. Prange, M. Gunji, C. E. D. Chidsey and P. C. McIntyre, *Energy Environ. Sci.*, 2013, **6**, 2487–2496.
15. M. Hettick, M. Zheng, Y. Lin, C. M. Sutter-Fella, J. W. Ager and A. Javey, *J. Phys. Chem. Lett.*, 2015, **6**, 2177–2182.
16. S. Hu, M. R. Shaner, J. A. Beardslee, M. Lichterman, B. S. Brunschwig and N. S. Lewis, *Science*, 2014, **344**, 1005–1009.
17. C. Rath, P. Mohanty, A. C. Pandey and N. C. Mishra, *J. Phys. D: Appl. Phys.*, 2009, **42**, 205101.
18. C. A. Hoffman, K. Jarašiūnas, H. J. Gerritsen and A. V. Nurmikko, *Appl. Phys. Lett.*, 1978, **33**, 536–539.
19. K. T. Fountaine, W.-H. Cheng, C. R. Bukowsky and H. A. Atwater, *ACS Photonics*, 2016, **3**, 1826–1832.

20. E. Aharon-Salom and A. Heller, *J. Electrochem. Soc.*, 1982, **129**, 2865–2866.
21. K. Shankar, J. I. Basham, N. K. Allam, O. K. Varghese, G. K. Mor, X. Feng, M. Paulose, J. A. Seabold, K.-S. Choi and C. A. Grimes, *J. Phys. Chem. C*, 2009, **113**, 6327–6359.
22. X. Yin, C. Battaglia, Y. Lin, K. Chen, M. Hettick, M. Zheng, C.-Y. Chen, D. Kiriya and A. Javey, *ACS Photonics*, 2014, **1**, 1245–1250.
23. S. W. Boettcher, E. L. Warren, M. C. Putnam, E. A. Santori, D. Turner-Evans, M. D. Kelzenberg, M. G. Walter, J. R. McKone, B. S. Brunschwig, H. A. Atwater and N. S. Lewis, *J. Am. Chem. Soc.*, 2011, **133**, 1216–1219.
24. A. Heller and R. G. Vadimsky, *Phys. Rev. Lett.*, 1981, **46**, 1153–1156.
25. J. R. McKone, A. P. Pieterick, H. B. Gray and N. S. Lewis, *J. Am. Chem. Soc.*, 2013, **135**, 223–231.
26. K. Gelderman, L. Lee and S. W. Donne, *J. Chem. Educ.*, 2007, **84**, 685.
27. P. P. Sahoo, B. Zoellner and P. A. Maggard, *J. Mater. Chem. A*, 2015, **3**, 4501–4509.
28. B. J. Morgan and G. W. Watson, *J. Phys. Chem. C*, 2010, **114**, 2321–2328.
29. K. Chandrasekaran and L. O. M. Bockris, *Surf. Sci.*, 1987, **185**, 495–514.
30. J. O. M. Bockris and J. C. Wass, *Mater. Chem. Phys.*, 1989, **22**, 249–280.
31. L. W. Diamond and N. N. Akinfiev, *Fluid Phase Equilib.*, 2003, **208**, 265–290.
32. J. Qiu, G. Zeng, P. Pavaskar, Z. Li and S. B. Cronin, *Phys. Chem. Chem. Phys.*, 2014, **16**, 3115–3121.
33. Y. Wang, I. Aravind, Z. Cai, L. Shen, G. N. Gibson, J. Chen, B. Wang, H. Shi, B. Song, E. Guignon, N. C. Cady, W. D. Page, A. Pilar and S. B. Cronin, *ACS Appl. Mater. Interfaces*, 2020, **12**, 17459–17465.
34. Y. Wang, L. Shen, Y. Wang, B. Hou, G. N. Gibson, N. Poudel, J. Chen, H. Shi, E. Guignon, N. C. Cady, W. D. Page, A. Pilar, J. Dawlaty and S. B. Cronin, *Faraday Discuss.*, 2019, **214**, 325–339.
35. M. L. Brongersma, N. J. Halas and P. Nordlander, *Nat. Nanotechnol.*, 2015, **10**, 25–34.
36. P. Narang, R. Sundararaman and H. A. Atwater, *Nanophotonics*, 2016, **5**, 96–111.
37. S.-M. Lee, W. Li, P. Dhar, S. Malyk, Y. Wang, W. Lee, A. Benderskii and J. Yoon, *Adv. Energy Mater.*, 2015, **5**, 1500761.
38. J. Chen, C. S. Bailey, Y. Hong, L. Wang, Z. Cai, L. Shen, B. Hou, Y. Wang, H. Shi, J. Sambur, W. Ren, E. Pop and S. B. Cronin, *ACS Photonics*, 2019, **6**, 787–792.
39. H. Shi, Z. Cai, J. Patrow, B. Zhao, Y. Wang, Y. Wang, A. Benderskii, J. Dawlaty and S. B. Cronin, *ACS Appl. Mater. Interfaces*, 2018, **10**, 33678–33683.

40. H. Shi, R. T. Pekarek, R. Chen, B. Zhang, Y. Wang, I. Aravind, Z. Cai, L. Jensen, N. R. Neale and S. B. Cronin, *J. Phys. Chem. C*, 2020, **124**, 17000–17005.
41. W. Hou, Z. Liu, P. Pavaskar, W. H. Hung and S. B. Cronin, *J. Catal.*, 2011, **277**, 149–153.
42. Z. Liu, W. Hou, P. Pavaskar, M. Aykol and S. B. Cronin, *Nano Lett.*, 2011, **11**, 1111–1116.
43. Z. Liu, W. H. Hung, M. Aykol, D. Valley and S. B. Cronin, *Nanotechnology*, 2010, **21**, 105304.
44. R. P. Van Duyne, J. C. Hulteen and D. A. Treichel, *J. Chem. Phys.*, 1993, **99**, 2101–2115.
45. S. Mukherjee, F. Libisch, N. Large, O. Neumann, L. V. Brown, J. Cheng, J. B. Lassiter, E. A. Carter, P. Nordlander and N. J. Halas, *Nano Lett.*, 2013, **13**, 240–247.
46. G. Tagliabue, J. S. DuChene, M. Abdellah, A. Habib, D. J. Gosztola, Y. Hattori, W.-H. Cheng, K. Zheng, S. E. Canton, R. Sundararaman, J. Sá and H. A. Atwater, *Nat. Mater.*, 2020, **19**, 1312–1318.
47. I. Aravind, Y. Wang, Z. Cai, L. Shen, B. Zhao, S. Yang, Y. Wang, J. M. Dawlaty, G. N. Gibson, E. Guignon, N. C. Cady, W. D. Page, A. Pilar and S. B. Cronin, *Crystals*, 2021, **11**, 118.
48. D. J. Boston, C. Xu, D. W. Armstrong and F. M. MacDonnell, *J. Am. Chem. Soc.*, 2013, **135**, 16252–16255.
49. E. Barton Cole, P. S. Lakkaraju, D. M. Rampulla, A. J. Morris, E. Abelev and A. B. Bocarsly, *J. Am. Chem. Soc.*, 2010, **132**, 11539–11551.
50. Y. Yan, E. L. Zeitler, J. Gu, Y. Hu and A. B. Bocarsly, *J. Am. Chem. Soc.*, 2013, **135**, 14020–14023.
51. J. Lloyd-Hughes, S. K. E. Merchant, L. Fu, H. H. Tan, C. Jagadish, E. Castro-Camus and M. B. Johnston, *Appl. Phys. Lett.*, 2006, **89**, 232102.
52. C.-C. Chang, C.-Y. Chi, M. Yao, N. Huang, C.-C. Chen, J. Theiss, A. W. Bushmaker, S. LaLumondiere, T.-W. Yeh, M. L. Povinelli, C. Zhou, P. D. Dapkus and S. B. Cronin, *Nano Lett.*, 2012, **12**, 4484–4489.
53. M. Pourbaix, *Atlas of Electrochemical Equilibria in Aqueous Solutions*, National Association of Corrosion Engineers, Houston, Texas, 1974.
54. E. McCafferty, in *Introduction to Corrosion Science*, ed. E. McCafferty, Springer, New York, NY, 2010, pp. 95–117, DOI: 10.1007/978-1-4419-0455-3_6.
55. J.-Y. Liu, X.-Q. Gong, R. Li, H. Shi, S. B. Cronin and A. N. Alexandrova, *ACS Catal.*, 2020, **10**, 4048–4058.
56. J.-Q. Li, L. Meng, M. Sprik and J. Cheng, *J. Phys. Chem. C*, 2020, **124**, 19003–19014.
57. J. T. Choy, J. D. B. Bradley, P. B. Deotare, I. B. Burgess, C. C. Evans, E. Mazur and M. Lončar, *Opt. Lett.*, 2012, **37**, 539–541.
58. C. C. Evans, C. Liu and J. Suntivich, *Opt. Express*, 2015, **23**, 11160–11169.

59. S. Yalamanchili, E. Verlage, W.-H. Cheng, K. T. Fountaine, P. R. Jahelka, P. A. Kempler, R. Saive, N. S. Lewis and H. A. Atwater, *Nano Lett.*, 2020, **20**, 502–508.
60. O. Khaselev and J. A. Turner, *Science*, 1998, **280**, 425.
61. E. Verlage, S. Hu, R. Liu, R. J. R. Jones, K. Sun, C. Xiang, N. S. Lewis and H. A. Atwater, *Energy Environ. Sci.*, 2015, **8**, 3166–3172.
62. P. Varadhan, H.-C. Fu, Y.-C. Kao, R.-H. Horng and J.-H. He, *Nat. Commun.*, 2019, **10**, 5282.
63. J. L. Young, M. A. Steiner, H. Döscher, R. M. France, J. A. Turner and T. G. Deutsch, *Nat. Energy*, 2017, **2**, 17028.
64. K. Sun, Y. Kuang, E. Verlage, B. S. Brunschwig, C. W. Tu and N. S. Lewis, *Adv. Energy Mater.*, 2015, **5**, 1402276.